Journal of Engineering Technology and Applied Physics

Figure-of-Merits (FOM) for Direct Current TENG (Triboelectric Nanogenerator): Structural vs Dimensionless

Mohamed Omer M. Abdelrahim[*], Lee Lini and Sin Yew Keong
Faculty of Engineering, Multimedia University, Cyberjaya, Selangor, Malaysia.
*Corresponding author: monjio45@gmail.com, *ORCiD*: 0009-0000-9884-7207
https://doi.org/10.33093/jetap.2023.5.2.13

Abstract — **This review paper provides a detailed overview of figure-of-merits (FOM) of Direct Current triboelectric nanogenerators (DC-TENGs). TENG represent a potentially ground-breaking technology for extracting mechanical energy from the environment. The FOM is a critical parameter that determines the efficiency of the energy conversion. This paper discusses the various working modes of DC-TENGs and also the research done to maximize output charge density. The review looks at recent different FOMs that could be formulated to improve the analysis of the performance and efficiency of TENGs more accurately. Finally, the paper concludes with a comparison between two different types of FOMs namely structural FOMs and dimensionless FOMs. It provides a valuable resource for researchers working in the field of TENGs and it sheds light on the key factors that influence the FOM of DC-TENGs. This enables the development of more efficient energy harvesting devices.**

Keywords—Triboelectric nanogenerators, Figure-of-merits, Energy conversion

I. INTRODUCTION

Triboelectric nanogenerators (TENGs) have become a significant topic of attention across studies conducted in converting mechanical energy into electrical in recent years. Among various types of TENGs, direct current TENGs (DC-TENGs), which operates in 4 different working modes, have emerged as an enticing innovation for harvesting energy from various mechanical sources because of its high output power, efficiency, and simplicity [1-6]. To analyze the performance of DC-TENGs, it is important to establish appropriate figures-of-merit (FOMs) that can quantify their energy conversion efficiency and power generation capability. In this review paper, we present a comprehensive analysis of various FOMs that have been proposed for DC-TENGs, including output voltage, power density, output current, and energy conversion efficiency. In addition to that, we compared two types of FOMs namely, structural FOMs and dimensionless FOMs. This review paper aims to provide a comprehensive understanding of the FOMs of DC-TENGs, which could benefit researchers and engineers in the field of harvesting energy and related applications.

II. BACKGROUND

A. Working Modes of TENG

DC-TENGs have 4 basic working modes: (1) contact-separation mode, (2) linear sliding mode, (3) single-electrode mode and (4) freestanding triboelectric layer mode.

B. Contact Separation Mode

The least complex operating mode is contact separation. Fig. 1 depicts its basic structure. When two or more materials having different electron affinities touch, the surfaces of those materials become electrically charged oppositely. A potential is formed at the interface between two surfaces upon separation as a result of an external force. In order to keep the electrostatic equilibrium, electrons then flow via the external circuit [7-10].
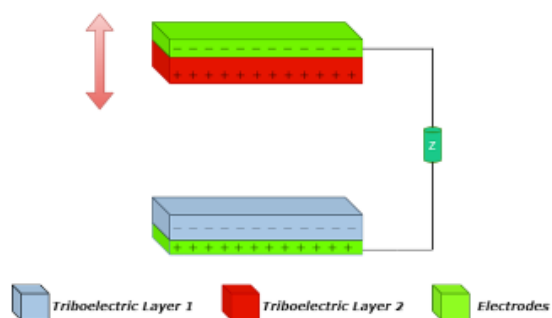
Fig. 1. Schematic diagram of a contact-separation mode TENG [11].

C. Linear Sliding Mode

Figure 2 depicts the fundamental configuration for a linear sliding mode. The contact area between the two components changes as they move past one another, which disturbs the electrostatic field balance and provides a potential that drives electrons across the external circuit [12]. The cycle of the process is similar to the contact-separation mode. Thus, many grating structures are built, each tailored to a different energy-gathering or quantitative-sensing purpose, all beginning with the same fundamentals of linear-sliding mode. However, constant rubbing reduces durability and functionality of the materials [8, 10].
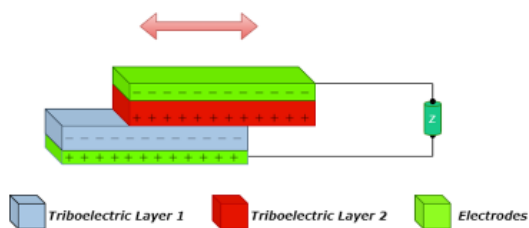

Fig. 2. Schematic diagram of a linear sliding mode TENG [11].

D. Single Electrode Mode

For linear sliding mode and contact-separation mode, both have their limitations in the fields of applications where the movable object is of primary interest, such as biological sensing and human-machine interfaces (HMIs). This is due to the need for a set of interconnected electrodes that moves relatively to one another. As shown in Fig. 3, the problem can be solved by using a single electrode that is directly connected to earth via a load. The dielectric layer (designated as triboelectric layer 2) is not connected electrically and is free to move. While moving in a vertical or lateral direction, the dielectric component transfers charges to and from the ground electrode. This mode allows for greater adaptability at the expense of output performance [8].
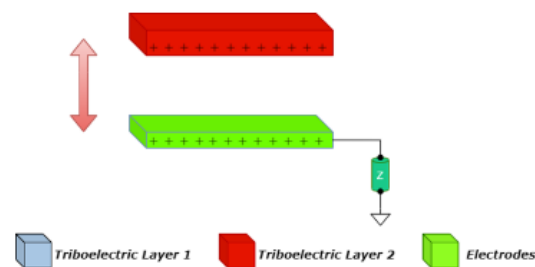

Fig. 3. Schematic diagram of a single-electrode mode TENG [11].

E. Freestanding Triboelectric Layer Mode

The freestanding triboelectric-layer mode keeps both electrodes stationary and not connected to the ground. Figure 4 shows the configuration of a basic freestanding triboelectric layer mode. It comprises of two symmetric electrodes connected together via a load. Induction creates an asymmetry in the distribution of charges when the dielectric component is moved between the electrodes, leading to a transfer of charges through the electrodes via the external load. The characteristics of this mode have inspired the creation of grating structures that are universally used for sliding motions [8].
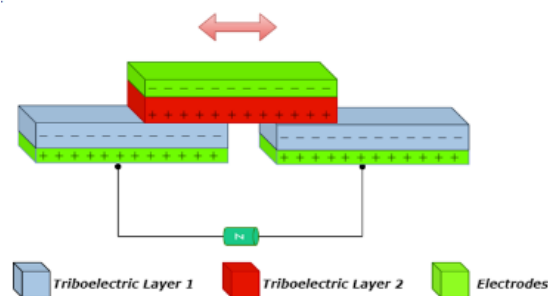

Fig. 4. Schematic illustration of a freestanding triboelectric layer mode TENG [11].

III. MAXIMIZING OUTPUT CHARGE DENSITY FROM DC-TENG

Several studies and experiments were made on improving the efficiency of DC-TENGs. This generally requires maximizing the output charge density. Three methods of improving output charge density of DC-TENGs are summarized in this paper. These methods are (1) Rationally patterned electrode (2) Electric double layer effect and (3) Charge shuttling.

A. Rationally Patterned Electrode of DC-TENG

To maximise output charge density from DC-TENGs by enhancing the efficiency of contact electrification [13, 14], Z. Zhao *et al.* [9] presented a microstructure-designed-direct-current TENG (MDC-TENG) with a rationally structured electrode structure.

Figure 5 depicts the proposed MDC-TENG architecture. Fine friction electrodes (FEs; usually a copper wire) and charge collecting electrodes (CCEs; usually a stainless-steel wire) are the main components of the system's architecture. The scanning electron micrograph (SEM) in Fig. 5(b) shows that each FE maintains a small separation from its surrounding

CCEs and that the same holds true for the separation of CCEs from the friction layer (polytetrafluoroethylene, PTFE) [9].
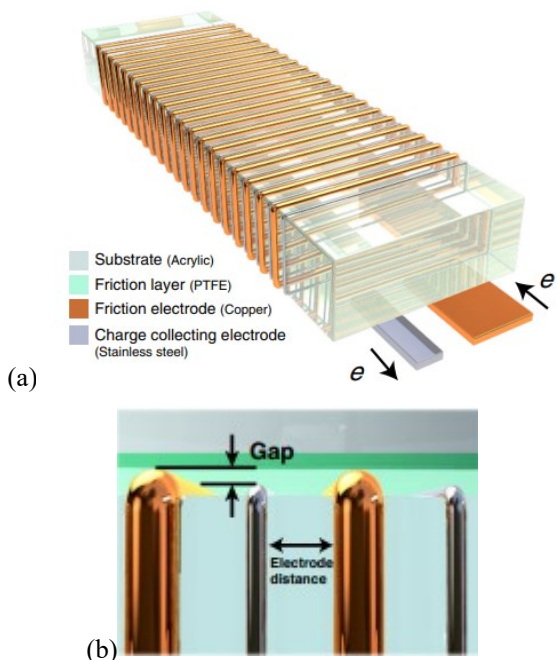

(a)

(b)

Fig. 5. Structural design of the proposed MDC-TENG (a) Schematic illustration (b) SEM image (scale bar: 500μm) [9].

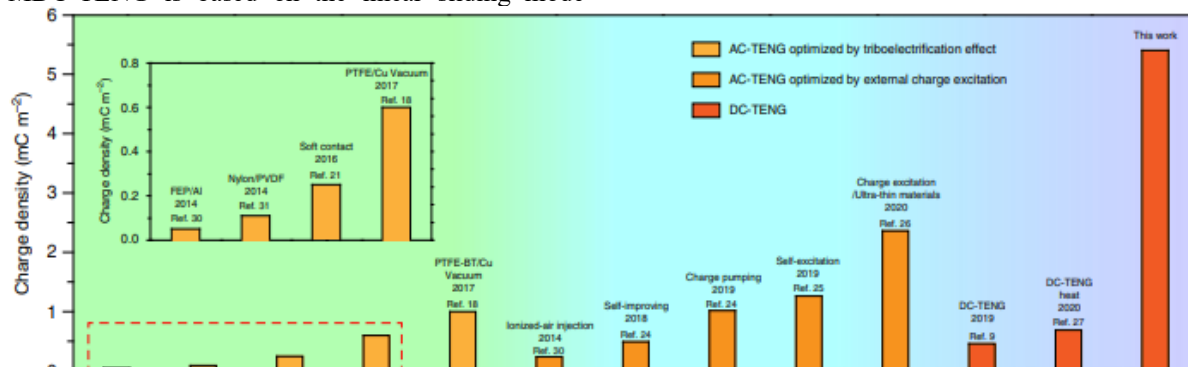The fundamental working mechanism behind the MDC-TENG is based on the linear sliding mode (rotary mode) since it relies on friction [13]. As the FE slides against the friction layer, electrons move from the FE to the friction layer due to the triboelectrification effect. A DC is produced due to the air breakdown between the charged friction layer and CCE. Figure 6 depicts the working mechanism of MDC-TENG [9].
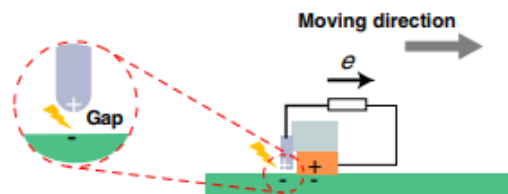

Fig. 6. Working mechanism of MDC-TENG [9].

Figure 7 shows a comparison of surface charge densities between other types of TENGs both AC or DC and MDC-TENG [13, 15, 16-24]. The results indicated a remarkable success for MDC-TENG in "This work" [9]. While this design seems to yield the highest charge density amongst other designs, a linear sliding (rotary mode) DC-TENG is not suitable for many applications such as smart watches, wearables, etc. A DC-TENG working in contact-separation mode or conventional sliding mode would be better in this aspect.

Fig. 7. A comparison of charge densities between MDC-TENG and other TENGs [9].

B. Electric Double Layer Effect

One way to enhance the surface charge density of TENGs is using the electric double layer proposed by J. Chun *et al.* [25]. Figure 8 shows a representation of the improved design. The TENG is constructed from three layers: a top electrode made of aluminium (Al) followed by a mesoporous polymer film (made of polydimethyl siloxane, PDMS), an Al film coated with Au nanoparticles as the middle layer and Al as the bottom layer. Better output power can be generated from a mesoporous film compared to a flat film [26]. Coating the Al film with Au nanoparticles improves its stability by increasing its surface contact area with the polymer layer and providing more protection from oxidation. A separation between the upper and intermediate levels was achieved with the help of four

springs that were fixed to the edges. Finally, an Al film bottom electrode was employed with springs to keep the separation distance constant between the layers, similar to the top electrode [25].

Figure 9 depicts the mechanism proposed by J. Chun [26]. A negative charge is induced on the mesoporous film upon initial contact with the positively charged surface of the intermediate layer, which is the result of an external force on the top layer. Both layers eventually make contact with the ground as a result of the applied force, but they do so in a specific order: the top layer first, then the bottom layer. All three layers unwind simultaneously once the pressure is released. Because of the induction of electron flow from ground by positive charges in the intermediate and top electrode by negative charges in

the porous film, electrons will flow via the external circuit [27]. The top electrode will be positively charged after one cycle, whereas the bottom electrode and porous sheet will be negatively charged [25].
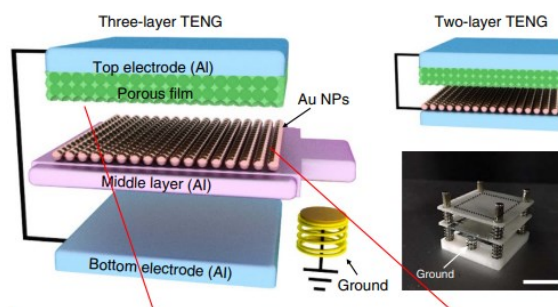

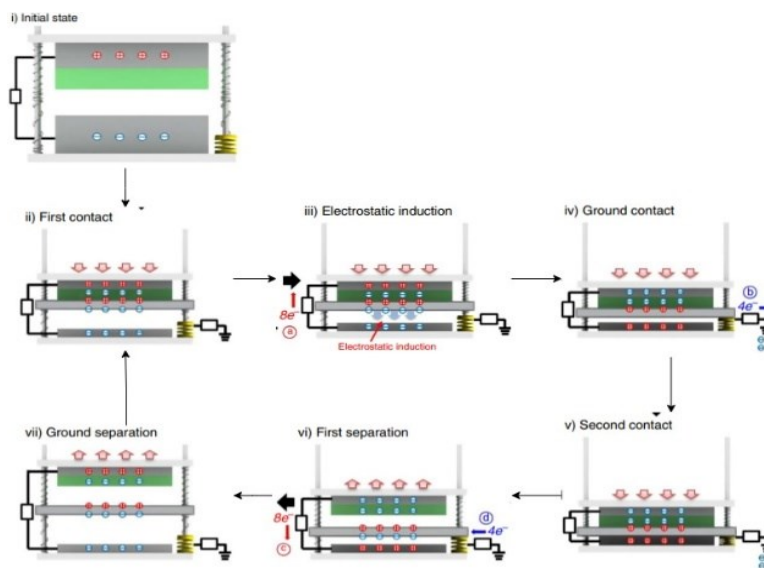Fig. 8. Schematic diagram of the proposed three-layer TENG [25].

Fig. 9. Working principle of the proposed three-layer TENG [25].

Three layered TENG seemed to have a better output performance as compared to conventional two-layered TENGs. This is depicted in Fig. 10. It's common approach that a TENG's output power increases linearly with the force applied [28]. Hence, with an applied external force of 50 N, the charge density of the three-layered TENG was 275.44 μCm^{-2} which is around 4.5 times that of a convention two-layered TENG which was around 60 μCm^{-2}. In addition, while rectifying the output AC signals using a diode bridge, the three-layered TENG achieved a charge density of up to 4600 mCm^{-2} [25].
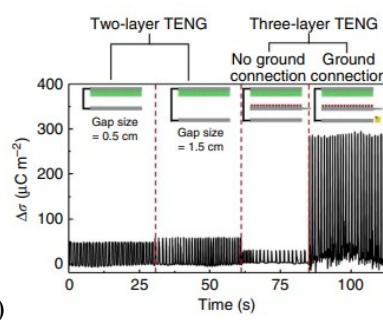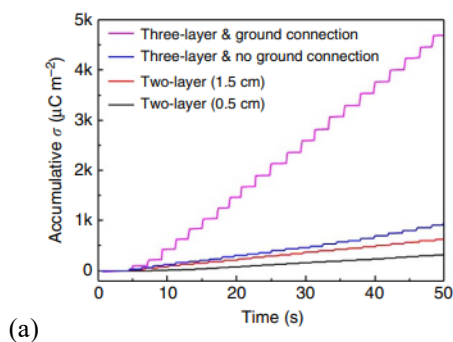

Fig. 10. (a) Output charge densities comparison between conventional two-layer TENGs and (b) the proposed three-layered TENG [25].

C. Charge Shuttling

H. Wang *et al.* presents a charge shuttling TENG (CS-TENG) in order to enhance the surface charge density [29]. CS-TENG presents a mechanism for charge shuttling between domains of conduction. When two quasi-symmetrical domains interact, charge carriers can be shuttled back and forth between them, thereby doubling the output. Concurrently, a charge pump efficiently generates charges serving as an operational medium in the domains. Under ambient conditions, a charge density of 1.85 mCm^{-2} is

achievable. H. Wang fabricated and characterized a high-performing CS-TENG based on integrated device [29]. This is for wave energy harvesting in in order to analyze the functionality and performance of the proposed method [29, 30].

The working principle of CS-TENG is depicted in Fig. 11. The CS-TENG consists of two conventional TENGs as well as a commercialized buffer capacitor [31, 32]. The main TENG electrodes and the electrodes of the buffer capacitor form a quasi-symmetrical structure with two conduction domains, one on the Q+ side and the other on the Q- side. Charges are injected into the domains via a rectifier, which must be able to tolerate high voltage (electronic extraction is similar to the injection of positive charge carriers). When the main TENG is contacted and then separated, differences in voltages are due to the intrinsic capacitances of the main TENG with the buffer capacitor. As a result, a nearly symmetrical charge exchanging would occur between the main TENG and the buffer capacitor, powering both loads [29, 33].
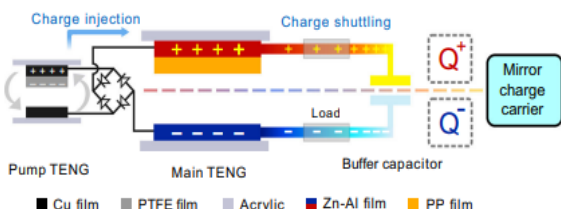

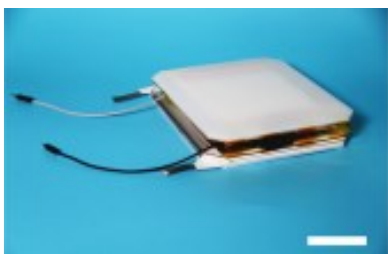Fig. 11. Working principle of CS-TENG [29].

Fig. 12. Fabricated CS-TENG [29].

Figure 12 shows the fabricated CS-TENG consisting of both the main TENG as well as the pump TENG stacked together. The main TENG used Zn-Al films for electrodes while a 5μm polypropylene (PP) is adopted as the dielectric layer. On the other hand, the pump TENG uses copper electrodes and PTFE as a dielectric layer. A 50nF capacitor is utilized as the buffer capacitor [29].

The resulting output performance of the fabricated CS-TENG is shown in Fig. 13 (b). Figure 13(a) shows that a projected surface charge density of 1.5 mCm^{-2} when a Zener diode is utilised to prevent dielectric breakdown between the two domains. To calculate the predicted charge density, we divide the combined output of both sides by the contact area. This is different from the more commonly used term "surface charge density," which is used when referring to

conventional TENGs. The predicted charge density with no Zener diode is 1.85 mCm^{-2} [19, 20].
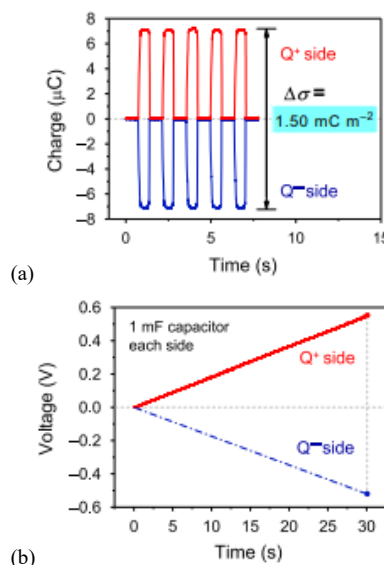
Fig. 13. Output performance of CS-TENG (a) resulting output charge and surface charge density (b) Illustration of charging two large capacitors simultaneously [29].
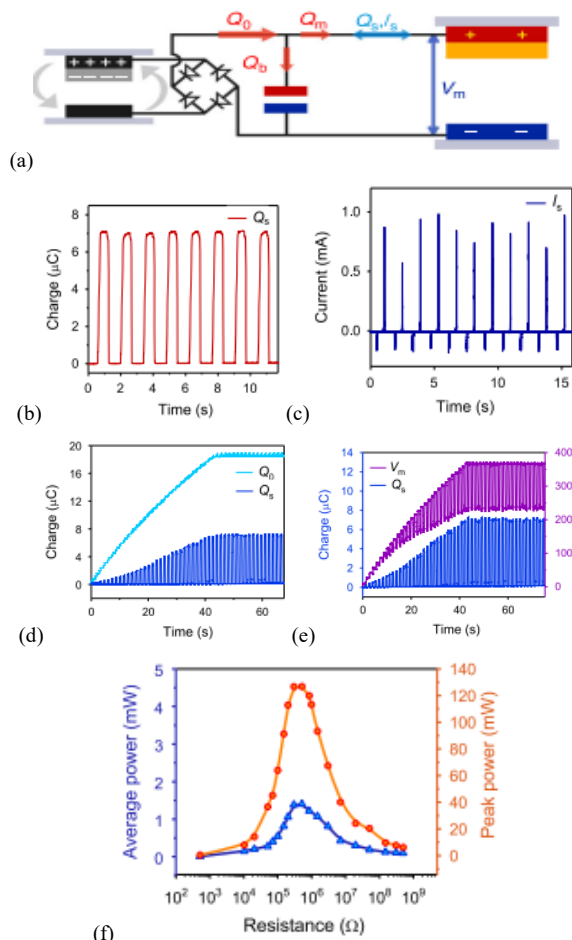

Fig. 14: CS-TENG output performance (a) Equivalent circuit diagram, (b) output shuttled charges, (c) current of CS-TENG, (d) Shuttled charges and simultaneously injected charges, (e) Shuttled charges and simultaneous voltage and (f) average power and peak output power [29].

Two 1 mF capacitors were charged to 0.54 V and 0.52 V respectively in 30 seconds at an agitation frequency of 1.43 Hz (Fig. 13b), after confirming the high yield and indicating that the output voltage is adequate to turn on electronic devices. Figure 14 shows the electrical circuit and the implementation of charge shuttling TENGs as well as the electrical output performance and charge obtained. The results suggest that the charge shuttling-based mechanical energy harvesting system CS-TENG is capable of generating very high output [29].

The design showed effectiveness but it is highly complicated and difficult to fabricate. Hence, having a simpler design with a higher output charge density is desired.

IV. FIGURE OF MERITS OF DC-TENGS

To numerically analyse TENG's performance from the perspectives of its structure and materials, Y. Zi *et al.* presented a standardised approach [34]. First, based on a plot of built-up voltage V vs total transferred charges, Y. Zi *et al.* discussed the optimum TENG operating cycle for maximum energy output. This led them to establish a cycle-based performance figure-of-merit (FOM$_P$) for TENG that accounts for both the structural FOM (FOM$_S$) associated with TENG design and the material FOM (FOM$_M$) that is proportional to the square of the surface charge density. The structural FOM is generated and simulated for each TENG setup in order to characterise and compare them. They proposed a unified approach to FOM quantification. Future TENG applications and industrialization can be found here [34].

Based on the relation of the accumulated voltage V, the charges transferred through the electrodes Q, and the triboelectric layer's relative displacement x, the governing equations of TENGs can be constructed. Y. Zi utilizes the widely used minimum achievable charge reference state (MACRS) [26, 33] to do this. Short circuit transmitted charges $Q_{SC(x)}$ and open circuit voltage $V_{OC(x)}$ are both zero at the $x = 0$ point. Figure 15 shows the displacement x and the two electrode definitions for a linear sliding mode TENG. When $x = x_{max}$, it is predicted that $Q_{SC(x)}$ and $V_{OC(x)}$ will both be at their highest values [34].
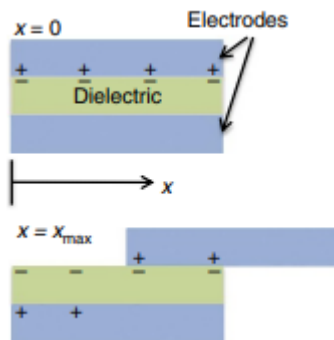

Fig. 15. Schematic diagram of a linear sliding mode TENG having a displacement $x = 0$ and $x = x_{max}$ [34].

The electrical signal generated is time-dependent, just like the underlying motion. In order to measure the efficiency of the TENG, its typical output power $\bar{P}$ is calculated, which varies with the load resistance. The output energy per cycle E over some time interval T is derived as:

$$E = \bar{P}T = \int_0^T VI\,dt = \int_{t=0}^{t=T} V\,dQ = \oint V\,dQ \qquad (1)$$

, where V refers to output voltage, I refers to output current and Q is output charge.

TENG's electrostatic states and energy generation can be depicted as a graph of accumulated voltage V vs transferred charges Q. Starting at (V, Q) = (0, 0), the simulated V-Q for a linear sliding (LS) mode TENG using the finite element method (FEM) with an external load resistance of 100 M is shown in Fig. 17. The specifics of this TENG linear sliding mode are detailed in Table I.

Table I: Simulation parameters used for LS TENG [34].

Dielectric effective thickness, $d_0 = \Sigma d_i/\varepsilon_{ri}$	90.8 μm
Triboelectrification area A (length l X width w)	8.5 X 7.9 cm
Maximum displacement, x_{max}	3.5 cm
Surface charge density, σ	12 μCm^{-2}

Based on the V-Q plot (Fig. 16), we may infer that the after a few cycles of operation, TENG will reach steady state. At the steady-state output, it is expected that the V-Q plot will be a closed loop as the steady-state output signal from TENG has a periodic response to mechanical triggering. The area under the curve in a voltage-current (V-Q) graph represents the energy output E, as shown in Eq. (1) [34]. Under varying external stresses, FEM simulations were also used to provide V-Q plots for the linear sliding mode TENG in steady state (Fig. 17).
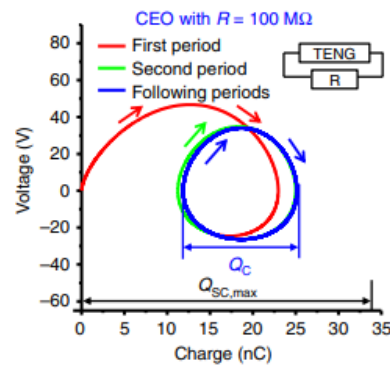

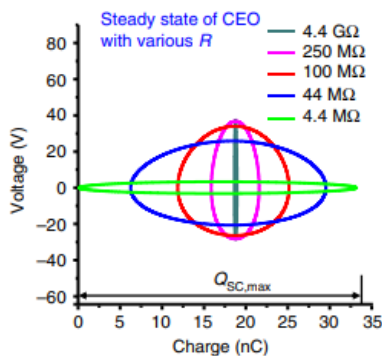Fig. 16. V-Q plot of the LS TENG [34].

Fig. 17. Steady state V-Q plot simulated by FEM [34].

The circular sections of the V-Q plots show that E is maximised when a matched load resistance is applied. "Cycles for Energy Output" (CEO) is the term for these intervals. Figure 16 shows that the difference between a CEO's maximum and minimum steady-state transmitted charges is equivalent to the total cycling charge QC for that CEO [34].

Figures 16 and 17 indicate that for cycles with high external load resistances, the maximum $Q_{SC,max}$ transferred by each CEO is greater than the total Q_C cycling charge. For certain cycles, E could benefit by setting $Q_C = Q_{SC,max}$. It was then calculated that under a short-circuit state, $Q_C = Q_{SC,max}$. Abruptly, procedures were devised to achieve short-circuit circumstances during operation. A switch as in Fig. 18, is connected in parallel with the external load to accomplish this.
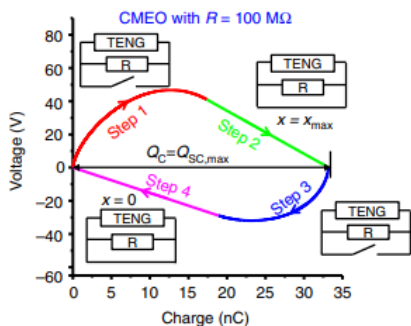

Fig. 18. CMEO with a load resistance R = 100 MΩ and $Q_C = Q_{SC, max}$ [34].

The workflow for the design is also shown in Fig. 18 and it follows the sequence from Step 1, at switch off, the triboelectric layer displaces from $x = 0$ to $x = x_{max}$; Step 2, enable $Q = Q_{SC, max}$ by turning on the switch and then turn it off; Step 3, in the transition from on to off, triboelectric layers shift from $x = x_{max}$ to $x = 0$ relatively; Step 4, switches on to make $Q = 0$ active, and then off again. Maximum total cycling charge of $Q_C = Q_{SC, max}$ was attained because transient short-circuit conditions in steps 2 and 4 were well controlled.

Figure 19 shows the simulation results of the design tested with different external load resistances. Y. Zi named these cycles as "cycles for maximized energy output" (CMEO). The CMEO clearly prove to

have higher output energy per cycle compared to CEO as shown in Figs. 18 and 19. Another observation was that for a higher external load resistance R, the E is higher. Thus, the open-circuit condition ($R = \infty$) yields the highest possible E. This condition of infinite load resistance is also shown in Fig. 19. This corresponding CMEO follows a trapezoid shape and the $Q_{SC, max}$ determine the vertices of this trapezoid. At $Q = Q_{SC,max}$, the graph shows that the absolute maximum voltage V_{max} and the maximum open circuit voltage $V_{OC, max}$ can be achieved. It was also demonstrated that the V-Q plots for all working modes of TENG are constrained within the bounds of this trapezium [34].
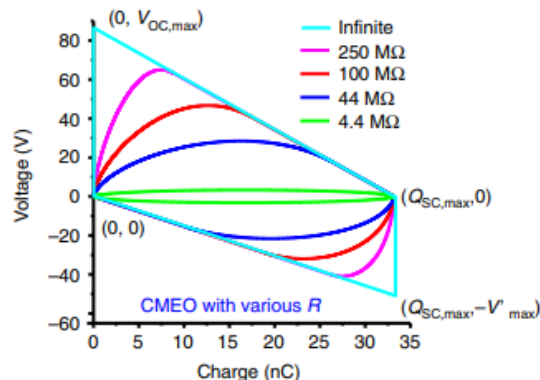
Fig. 19. CMEO under different load resistances [34].

For this reason, the following equation is utilized to determine the maximum possible output energy, E_m for this cycle, which has the largest encircled area:

$$E_m = \tfrac{1}{2} Q_{SC,max}(V_{OC,max} + V'_{max}) \qquad (2)$$

, where $V_{OC,max}$ refers to maximum open circuit voltage, $Q_{SC,max}$ is the maximum short circuit charges and V'_{max} is the maximum absolute voltage.
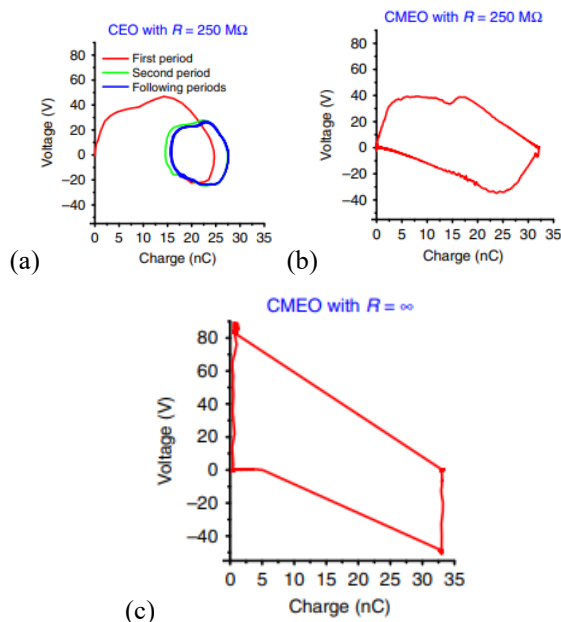
Fig. 20: Experimental results of CEO and CMEOs (a) V-Q plot of CEO with R=250MΩ (b) V-Q plot of CMEO with R=250MΩ (c) V-Q plot of CMEO with R=∞ [34].

The research conducted showed that CEO and CMEO are experimentally achievable. To do this, a linear sliding TENG is developed using the variables in Table I. The moving electrode was an Al foil and the second electrode was Cu deposited on a FEP film. The first demonstration of a V-Q plot for a CEO is shown in Fig. 20(a). It used an external resistance of 250 MΩ. It was found that it took a few operational periods for the CEO to settle into a steady state. Figs. 20(b) and 20(c) demonstrated the V-Q plot of CMEO with resistance values of 250 MΩ and ∞ respectively, using a series-controlled switch [34].

The V-Q plots obtained experimentally agreed well with those obtained through simulation (Figs. 16–19). Table II displays the results of an application of Eq. (1) to determine the energy output per cycle.

Table II: Output energy per cycle obtained for the three cycles of operation in the linear sliding mode [34].

Cycle type	Output energy per cycle (μJ)
CMEO with R = +∞	1.99
CMEO with R = 250 MΩ	1.48
CEO with R = 250 MΩ	0.47

These results further prove that CMEO with $R = \infty$ yields the maximum output energy per cycle [34]. For the TENG with $R = \infty$ in CMEO, the time T is split in two movements; TENG's relative movement and the discharging procedure under a short-circuit. Since resistance is very low in a short circuit, the second term of T can be greatly reduced or removed (less than 0.4 ms according to study) [35]. Therefore, the CMEO average output power $\bar{P}$ must meet:

$$\bar{P} = \frac{E_m}{T} \approx \frac{E_m}{2\frac{x_{max}}{\bar{v}}} = \frac{\bar{v}}{2}\frac{E_m}{x_{max}} \tag{3}$$

, where $\bar{v}$ is the relative motion of TENGs.

The relative motion of TENGs, $\bar{v}$, is proportional to the mechanical motions that drive it. The only variable in this equation that is related to TENG characteristics is E_m/x_{max}.

The TENGs energy conversion efficiency at CMEO with $R = \infty$ can be written as:

$$\eta = \frac{E_{out}}{E_{in}} = \frac{E_{output\ per\ cycle}}{E_{output\ per\ cycle} + E_{dissipation\ per\ cycle}}$$

$$= 1 / \left[1 + 1/\left(\frac{E_m}{2\bar{F}x_{max}}\right)\right] \tag{4}$$

, where $\bar{F}$ is the standard dissipative force produced by TENG. Drag, friction, and other similar forces fall under this category. The characteristics of TENG determine both the average power and the efficiency with which energy is converted, and both can be calculated using the term E_m/x_{max} in Eqs. (6) and (7). From Eq. (5), the triboelectrification area, A is directly proportional to the $Q_{SC,max}$ in E_m. To remove the effect of TENG's size on the output energy, we must use the area A as the denominator of this expression. For the

aforementioned explanation, we affirm that the term E_m/Ax_{max} is used to evaluate the merits of TENGs [34].

Using Eq. (2), it was determined E_m was directly proportional to the squared of surface charge density σ^2 since V'_{max}, $Q_{SC,max}$, and $V_{OC,max}$ are all proportional to σ^2. Since the factor is independent of any other variables besides the structural parameters and x_{max}, the structural FOM (FOM$_S$) (dimensionless) of TENG can be defined as:

$$\text{FOM}_S = \frac{2\varepsilon_0}{\sigma^2}\frac{E_m}{Ax_{max}} \tag{5}$$

, where ε_0 represents the permittivity of vacuum. The performance FOM (FOM$_P$) can be written as:

$$\text{FOM}_P = \text{FOM}_S.\sigma^2 = 2\varepsilon_0\frac{E_m}{Ax_{max}} \tag{6}$$

, where σ^2 corresponds to the material figure of merits (FOM$_M$), the only material-specific factor. Since the FOM$_P$ is related to the highest possible energy-conversion efficiency and the highest possible average output power, it can be viewed as the universal standard by which all modes and sizes of TENGs are analyzed.

A. Structural FOM of Different Modes of TENGs

Four different TENG modes of operation are compared in terms of their underlying structural architectures [34]. Comparisons of the structural designs of TENGs operating in contact separation (CS) mode, linear sliding (LS) mode, single electrode contact (SEC) structure in single electrode mode, sliding freestanding (SFT) and contact freestanding triboelectric (CFT) layer structures in FT mode were made using the finite element method (FEM). A comparison of the five structures' FOMs determined for varying values of the maximum displacement x_{max} are shown in Fig. 21.
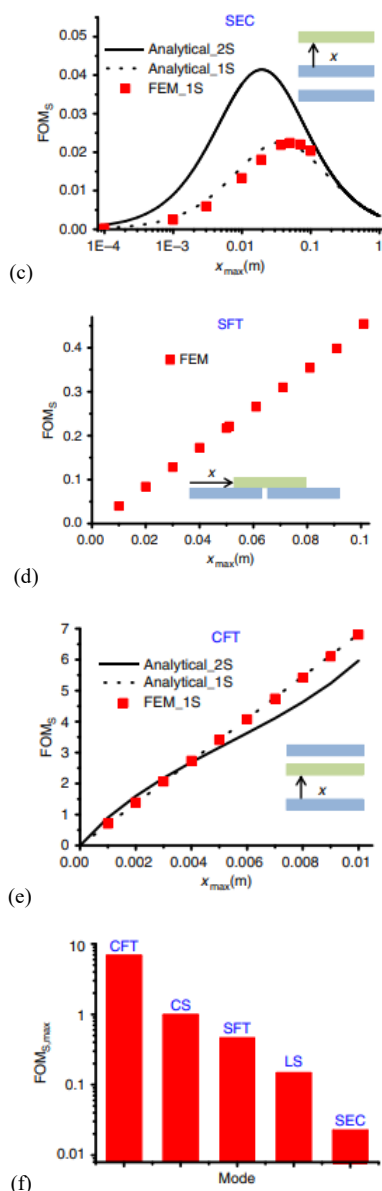
(a)

(b)
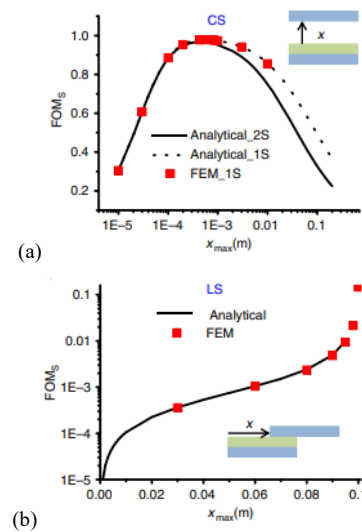
Fig. 21. FOM_S vs x_{max} for TENG structures (a) CS mode (b) LS mode (c) SEC mode (d) SFT mode (e) CFT mode (f) a comparison of the maximum FOM ($FOM_{S, max}$) of the different modes [34].

Non-ideal parallel-plate capacitances were calculated for the CS, SEC, and CFT structures using analytical procedures [34]. The computed findings agreed with those acquired through simulation. Therefore, the FEM simulations can be utilised to derive the highest value of structural FOM ($FOM_{S, max}$), which can then be used as a benchmark for evaluating the structures. Table III provides a concise overview of the $FOM_{S, max}$.

Table III: Results of simulated $FOM_{S, max}$ [34].

Structure	$FOM_{S, max}$
CFT	6.81
CS	0.98
SFT	0.45
LS	0.15
SEC	0.022

From Fig. 21 and Table III, it can be clearly concluded that the $FOM_{S, max}$ for TENGs decreases according to structures:

$$CFT > CS > SFT > LS > SEC$$

Multiple conclusions can be made from this study. To begin, the paired-electrode TENGs have been found to function better than SE TENGs despite being of similar size and material composition [36]. This is because the SE TENGs have low internal voltages and little amounts of transmitted charge. The second is that the efficiency of TENG triggered by CS action is higher than that of TENG induced by sliding if the triboelectric charge densities formed by the two processes are comparable. This is because a larger separation distance by sliding is necessary to achieve the same $V_{OC, max}$, resulting in a smaller $FOM_{S, max}$ [34]. In the freestanding mode, the capacitance decreases between electrodes while the performance enhances. During operation, the double-sided triboelectrification of the middle dielectric layer induces large transferred charges, which contribute to the high $FOM_{S, max}$ in the CFT structure [34].

B. Dimensionless FOM_M

Since the FOM_P is proportional σ^2, increasing σ improves the output of the TENG. As indicated, σ is the only variable that depends on the material on the FOM_P as indicated by Eq. (6). This density of surface charges is related to the triboelectric characteristics of the contacting materials. New studies show that surface roughness on the nanometer to micrometre scale has a direct effect on triboelectric performance [10, 13, 14, 37-39]. It was then determined that solid-to-solid contact prevents TENGs from achieving maximum surface charge density. Hence, Y. Zi *et al.* decided to use liquid metals such as liquid gallium, galinstan, and mercury as the triboelectrification materials. Since liquid metals are capable of taking on the shape of the solid surfaces which come into contact with. It is believed that the contact intimacy could be greatly improved with their uses. In one of the studies, galinstan, and non-toxic liquid gallium were used to analyze the surface charge density for a liquid electrode. To prevent quick oxidation of any gallium-containing liquid metals, experiments were carried out in a glove box at ambient temperature, 1 atm, and 0.006% relative humidity. The experimental set up is shown in Fig. 22.
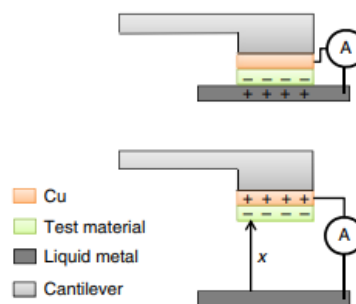

Fig. 22. Experimental design of TENG with liquid metal [34].

Liquid gallium or liquid gallinstan was used as one electrode while a Cu thin coating was deposited on the substance to be examined. Both the surfaces of the materials and the liquid metal became electrically charged due to the triboelectrification effect. In short circuit condition, if the Cu electrode is being charged high enough, practically all of the charges induced due to triboelectrification are transferred to the Cu electrode. Measuring the quantity of the charges, the surface charge density can be calculated. Instead of using liquid metals, solid gallium was utilised as an electrode to obtain a comparable reading for charge density. Y. Zi evaluated this model on a variety of materials including FEP, polyethylene (PE), Kapton, etc. It was found that the charge transfer was reliably replicable across numerous contact separation processes [34]. Figures 23(a) and (b) display these outcomes.
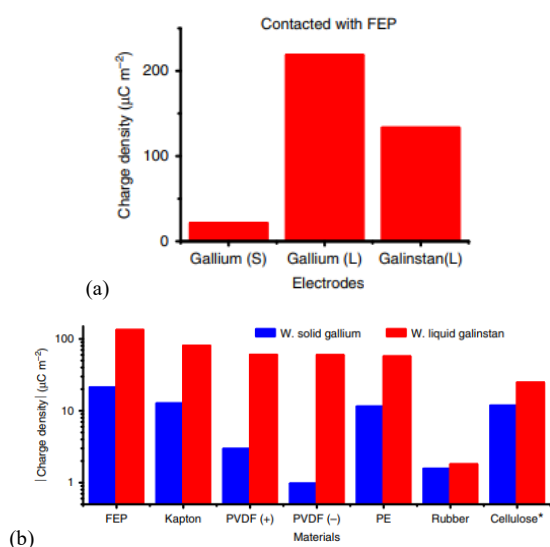

(a)

(b)

Fig. 23. Obtained experimental results for a liquid electrode TENG (a) Measured charge density when using FEP as a triboelectric layer against solid gallium, liquid gallium, and liquid gallinstan electrodes (b) Measured absolute charge density when using different triboelectric layer materials against solid gallium and liquid gallinstan [34].

When the examined material is more negatively charged than the liquid metal (like cellulose), the charge density will become positive and vice versa. The results also confirmed that materials tested against liquid metal electrodes yielded higher charge densities compared to materials tested against solid electrodes due to the enhanced contact intimacy as discussed previously. In a different study by Tang W *et al.* [14], it was also found that mercury yields the highest surface charge density compared to liquid gallium and gallinstan. Different liquid metals may have different capacities to absorb the electrons, which could have explained why measuring the charge density of the same material after coming into contact with them yields such different results.

A material's triboelectric performance is often measured in terms of the charge density of the surface in comparison to a liquid metal. Triboelectric

performance of FEP, σ_{FEP} when measured against a galinstan electrode, can be stated as $\sigma_{FEP}/\text{galinstan} = 133.24\ \mu\text{Cm}^{-2}$, and when tested against liquid gallium, it can be stated as $\sigma_{FEP}/\text{Ga(L)} = 218.64\ \mu\text{Cm}^{-2}$.

FEP is generally considered as the most negatively charged triboelectric material, whereas gallinstan is in a middle range. Therefore, the triboelectric charge densities measured while galinstan is in contact with FEP can be used as a standard reference. Consequently, for triboelectrification, the dimensionless material FOM (FOM_{DM}) and normalized triboelectric charge density σ_N are defined as follows:

$$\text{FOM}_{DM} = (\sigma_N)^2 = \frac{\sigma^2{}_{\text{Material/Galinstan}}}{\sigma^2{}_{\text{FEP/Galinstan}}}$$

(1)

Table IV lists the triboelectric charge densities and FOM_{DM} of the materials [34].

Table IV: σ_N and FOM_{DM} for different materials [34].

Materials	Normalized triboelectric charge density	Dimensionless material FOM
FEP	1	1
Kapton	0.6	0.36
Polyvinylidene fluoride (PVDF)	0.45	0.20
Polyethylene (PE)	0.43	0.18
Rubber	0.0135	0.000183
Galinstan	0	0
Cellulose	- 0.185	0.0342

V.   CONCLUSION

In conclusion, the benefits and drawbacks of various operational modes in DC-TENGs have been explored in this review. In addition, the paper dives into the number of variables that influence TENG performance and highlights the many approaches taken by prior studies to optimise the TENG's output charge density and, its performance.

In addition to that, a few figure-of-merits derived in research were presented in this paper and were used to quantify factors affecting TENG's performance. Important FOM for TENGs can be derived from the relationship between the built-up voltage V, the transferred charges between the electrodes Q, and the relative displacement between the triboelectric layers x. The type of materials, structural design, as well as natural form greatly influence the surface charge density, which is shown to be the main factor affecting the performance of TENGs.

Two significant types of FOMs can be extracted, namely; Structural FOM_S, and dimensionless material FOM_{DM}. Structural FOM is expressed as the ratio of the output voltage squared to the surface area of the TENG, normalized by the thickness of the device. Structural FOMs take into account the physical

characteristics of the device, such as its size and thickness and is dependent upon parameters such as dielectric constant of the materials used, shape and size of the contact surfaces, as well as the configuration of the electrodes. This applied mostly to solid materials with defined dimensions. Recent studies have shown that the structural configuration and surface roughness of the materials used could be a negative factor that affects the surface charge density of a TENG. Hence, it was determined that using liquid metals as triboelectrification materials would yield higher surface charge density and consequently enhancing the performance of TENGs. So, to mathematically formulate the figure-of-merits of this TENG, FOM$_{DM}$ has been extracted. FOM$_{DM}$ provides a normalized measure of the device's energy conversion efficiency. Results showed that using dimensionless materials like liquid metal as triboelectric materials leads to a much better TENGs.

Finally, based on this review, we will be formulating a FOM for the contact-separation mode DC-TENG. The focus will be on maximizing its output performance in CS mode and validate the FOM. This should enable the development of more efficient energy harvesting devices.

ACKNOWLEDGEMENT

REFERENCES

[1] J. Peng, S. D. Kang and G. J. Snyder, "Optimization Principles and the Figure of Merit for Triboelectric Generators," *Sci. Adv.*, vol. 3, no. 12, pp. eaap8576, 2017.

[2] Z. L. Wang and A. C. Wang, "On the Origin of Contact-electrification," *Mater. Today*, vol. 30, pp. 34–51, 2019.

[3] Q. T. Nguyen, C. P. Vo, T. H. Nguyen and K. K. Ahn, "A Direct-current Triboelectric Nanogenerator Energy Harvesting System Based on Water Electrification for Self-Powered Electronics," *Appl. Sci.*, vol. 12, no. 5, pp. 2724, 2022.

[4] Z. L. Wang, "On Maxwell's Displacement Current for Energy And Sensors: The Origin of Nanogenerators," *Mater. Today*, vol. 20, no. 2, pp. 74–82, 2017.

[5] Z. L. Wang, T. Jiang and L. Xu, "Toward the Blue Energy Dream by Triboelectric Nanogenerator Networks," *Nano Energ.*, vol. 39, pp. 9–23, 2017.

[6] C. Fang, T. Tong, T. Bu, Y. Cao, S. Xu, Y. Qi and C. Zhang, "Overview of Power Management for Triboelectric Nanogenerators," *Adv. Intell. Sys.*, vol. 2, no. 2, pp. 1900129, 2020.

[7] S. Niu, S. Wang, L. Lin, Y. Liu, Y. S. Zhou, Y. Hu and Z. L. Wang, "Theoretical Study of Contact-Mode Triboelectric Nanogenerators As An Effective Power Source," *Energ. Environ. Sci.*, vol. 6, no. 12, pp. 3576, 2013.

[8] X. Pu, S. An, Q. Tang, H. Guo and C. Hu, "Wearable Triboelectric Sensors for Biomedical Monitoring and Human-machine Interface," *iSci.*, vol. 24, no. 1, pp. 102027, 2021.

[9] Z. Zhao, Y. Dai, D. Liu, L. Zhou, S. Li, Z. L. Wang and J. Wang, "Rationally Patterned Electrode of Direct-Current Triboelectric Nanogenerators for Ultrahigh Effective Surface Charge Density," *Nat. Commun.*, vol. 11, no. 6186, 2020.

[10] Z. L. Wang, "Triboelectric Nanogenerators As New Energy Technology for Self-Powered Systems and As Active Mechanical and Chemical Sensors," *ACS Nano*, vol. 7, no. 11, pp. 9533–9557, 2013.

[11] M. O. Abdelrahim and L. Lee, "Design of DC-triboelectric Nanogenerator for Energy Harvesting," *Int. J. Technol.*, vol. 13, no. 6, pp. 1308-1316, 2022.

[12] S. Niu, Y. Liu, S. Wang, L. Lin, Y. S. Zhou, Y. Hu, and Z. L. Wang, "Theory of Sliding-mode Triboelectric Nanogenerators," *Adv. Mater.*, vol. 25, no. 43, pp. 6184–6193, 2013.

[13] D. Liu, X. Yin, H. Guo, L. Zhou, X. Li, C. Zhang, J. Wang and Z. L. Wang, "A Constant Current Triboelectric Nanogenerator Arising from Electrostatic Breakdown," *Sci. Adv.*, vol. 5, no. 4, pp. eaav6437, 2019.

[14] L. Zhou, D. Liu, S. Li, Z. Zhao, C. Zhang, X. Yin, L. Liu, S. Cui, Z. L. Wang, and J. Wang, "Rationally Designed Dual-mode Triboelectric Nanogenerator for Harvesting Mechanical Energy By Both Electrostatic Induction and Dielectric Breakdown Effects," *Adv. Energ. Mater.*, vol. 10, no. 24, pp. 2000965, 2020.

[15] J. Wang, C. Wu, Y. Dai, Z. Zhao, A. Wang, T. Zhang and Z. L. Wang, "Achieving Ultrahigh Triboelectric Charge Density for Efficient Energy Harvesting," *Nat. Commun.*, vol. 8, no. 88, 2017.

[16] J. Wang, S. Li, F. Yi, Y. Zi, J. Lin, X. Wang, Y. Xu and Z. Lin Wang, "Sustainably Powering Wearable Electronics Solely By Biomechanical Energy," *Nat. Commun.*, vol. 7, no. 12744, 2016.

[17] C. Zhang, L. Zhou, P. Cheng, Y. G. Xing, D. Liu, Xinyuan, L. H. Guo, Z. L. Wang and J. Wang, "Surface Charge Density of Triboelectric Nanogenerators: Theoretical Boundary and Optimization Methodology," *Appl. Mater. Today*, vol. 18, pp. 100496, 2020.

[18] L. Cheng, Q. Xu, Y. Zheng, X. Jia and Y. Qin, "A self-improving Triboelectric Nanogenerator with Improved Charge Density and Increased Charge Accumulation Speed," *Nat. Commun.*, vol. 9, no. 3773, 2018.

[19] L. Xu, T. Z. Bu, X. D. Yang, C. Zhang and Z. L. Wang, "Ultrahigh Charge Density Realized By Charge Pumping At Ambient Conditions for Triboelectric Nanogenerators," *Nano Energ.*, vol. 49, pp. 625–633, 2018.

[20] W. Liu, Z. Wang, G. Wang, G. Liu, J. Chen, X. Pu, Y. Xi, X. Wang, H. Guo, C. Hu and Z. L. Wang, "Integrated Charge Excitation Triboelectric Nanogenerator," *Nat. Comm.*, vol. 10, no. 1426, 2019.

[21] Y. Liu, W. Liu, Z. Wang, W. He, Q. Tang, Y. Xi, X. Wang, H. Guo and C. Hu, "Quantifying Contact Status and The Air-Breakdown Model of Charge-Excitation Triboelectric Nanogenerators to Maximize Charge Density," *Nat. Comm.*, vol. 11, no. 1599, 2020.

[22] D. Liu, L. L. Zhou, S. X. Li, Z. H. Zhao, X. Yin, Z. Y. Yi, C. L. Zhang, X. Y. Li, J. Wang and Z. L. Wang, "Hugely Enhanced Output Power of Direct-Current Triboelectric Nanogenerators By Using Electrostatic Breakdown Effect," *Adv. Mater. Technol.*, vol. 5, no. 7, pp. 2000289, 2020.

[23] S. Wang, Y. Xie, S. Niu, L. Lin, C. Liu, Y. S. Zhou and Z. L. Wang, "Maximum Surface Charge Density for Triboelectric Nanogenerators Achieved By Ionized-Air Injection: Methodology and Theoretical Understanding," *Adv. Mater.*, vol. 26, no. 39, pp. 6720–6728, 2014.

[24] Z. Wang, L. Cheng, Y. Zheng, Y. Qin and Z. L. Wang, "Enhancing the Performance of Triboelectric Nanogenerator Through Prior-Charge Injection and Its Application on Self-Powered Anticorrosion," *Nano Energ.*, vol. 10, pp. 37–43, 2014.

[25] J. Chun, B. U. Ye, J. W. Lee, D. Choi, C.-Y. Kang, S.-W. Kim, Z. L. Wang and J. M. Baik, "Boosted Output Performance of Triboelectric Nanogenerator via Electric Double Layer Effect," *Nat. Commun.*, vol. 7, no. 12985, 2016.

[26] J. Chun, J. W. Kim, W. S. Jung, C. Y. Kang, S. W. Kim, Z. L. Wang and J. M. Baik, "Mesoporous Pores Impregnated with Au Nanoparticles As Effective Dielectrics for Enhancing Triboelectric Nanogenerator Performance in Harsh Environments," *Energ. Environ. Sci.*, vol. 8, no. 10, pp. 3006–3012, 2015.

[27] T. H. Fay and S. D. Graham, "Coupled Spring Equations," *Int. J. Math. Edu. in Sci. and Technol.*, vol. 34, no. 1, pp. 65–79, 2003.

[28] G. Zhu, Z. H. Lin, Q. Jing, P. Bai, C. Pan, Y. Yang, Y. Zhou and Z. L. Wang, "Toward Large-scale Energy Harvesting By A Nanoparticle-Enhanced Triboelectric Nanogenerator," *Nano Lett.*, vol. 13, no. 2, pp. 847–853, 2013.

[29] H. Wang, L. Xu, Y. Bai, and Z. L. Wang, "Pumping Up the Charge Density of A Triboelectric Nanogenerator By Charge-Shuttling," *Nat. Commun.*, vol. 11, no. 4230, 2020.

[30] H. Wu, S.Fu, W. He, C. Shan, J. Wang, Y. Du, S. Du and B. Li, "Improving and Quantifying Surface Charge Density via Charge Injection Enabled By Air Breakdown," *Adv. Funct. Mater.*, vol. 32, no. 35, pp. 2203884, 2022.

[31] Z. L. Wang, J. Chen and L. Lin, "Progress in Triboelectric Nanogenerators As A New Energy Technology and Self-Powered Sensors," *Energ. Environ. Sci.*, vol. 8, no. 8, pp. 2250–2282, 2015.

[32] S. Niu and Z. L. Wang, "Theoretical Systems of Triboelectric Nanogenerators," *Nano Energ.*, vol. 14, pp. 161–192, 2015.

[33] J. Luo, L. Xu, W. Tang, T. Jiang, F. R. Fan, Y. Pang, L. Chen, Y. Zhang and Z. L. Wang, "Direct-current Triboelectric Nanogenerator Realized By Air Breakdown Induced Ionized Air Channel*," Adv. Energ. Mater.*, vol. 8, no. 27, pp. 1800889, 2018.

[34] Y. Zi, S. Niu, J. Wang, Z. Wen, W. Tang and Z. L. Wang, "Standards and Figure-of-Merits for Quantifying the Performance of Triboelectric Nanogenerators," *Nat. Commun.*, vol. 6, no. 8376, 2015.

[35] G. Cheng, Z. H. Lin, L. Lin, Z. Du and Z. L. Wang, "Pulsed Nanogenerator with Huge Instantaneous Output Power Density," *ACS Nano*, vol. 7, no. 8, pp. 7383–7391, 2013.

[36] S. Niu, Y. Liu, S. Wang, L. Lin, Y. S. Zhou, Y. Hu and Z. L. Wang, "Theoretical Investigation and Structural Optimization of Single-Electrode Triboelectric Nanogenerators," *Adv. Funct. Mater.*, vol. 24, no. 22, pp. 3332–3340, 2014.

[37] H. T. Baytekin, A. Z. Patashinski, M. Branicki, B. Baytekin, S. Soh and B. A. Grzybowski, "The Mosaic of Surface Charge in Contact Electrification," *Sci.*, vol. 333, no. 6040, pp. 308–312, 2011.

[38] T. A. L. Burgo, T. R. D. Ducati, K. R. Francisco, K. J. Clinckspoor, F. Galembeck and S. E. Galembeck, "Triboelectricity: Macroscopic Charge Patterns Formed By Self-Arraying Ions on Polymer Surfaces," *Langmuir*, vol. 28, no. 19, pp. 7407–7416, 2012.

[39] W. Tang, T. Jiang, F. R. Fan and A. F. Yu, "Liquid-metal Electrode for High-Performance Triboelectric Nanogenerator At An Instantaneous Energy Conversion Efficiency of 70.6%," *Adv. Funct. Mater.*, vol. 25, no. 24, pp. 3718–3725, 2015.